



pubs.acs.org/JPCC Article

# Oxygen Vacancies Altering the Trapping in the Proton Conduction Landscape of Doped Barium Zirconate

Published as part of The Journal of Physical Chemistry virtual special issue "Lawrence R. Pratt Festschrift". Ziqing Lin, Shiyun Lin, Yuan Tian, Alice Van Bokkelen, Maryann Valerio, and Maria A. Gomez\*



Cite This: J. Phys. Chem. C 2020, 124, 27954-27964

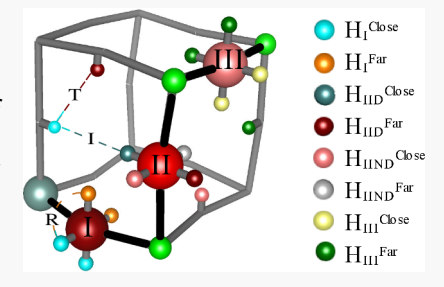


**ACCESS** 

III Metrics & More

Article Recommendations

ABSTRACT: Acceptor-doped barium zirconate is one of the most promising proton conducting materials for stationary hydrogen fuel cells. Dopant-defect proton traps shape the proton conduction landscape. Inspired by findings that oxygen vacancies may decrease trapping near some dopant defects (*Chem. Mater.* 2018, 30, 4919–4925), the effect of oxygen vacancies on the proton conduction landscape of barium zirconate is explored at 12.5% doping with aluminum, scandium, and yttrium dopant at the zirconium site. Density functional theory (DFT) with the PBE functional in the Vienna ab initio simulation package (VASP) was used to find the electronic energy for barium zirconate configurations. The conjugate-gradient minimization method is used to find the lowest energy structures and the climbing nudged elastic band (cNEB) method is used to find



transition states. As the dopant (D) ion radius increases, the lattice size expands from 4.24 to 4.29 Å and increases  $DO_6$  octahedral tilting in barium zirconate. Inclusion of an oxygen vacancy broadens ZrOD and ZrOZr angle distributions. While there are three distinct minima for oxygen vacancy locations, relative energies of minima and transition states show that only the dopant nearest neighbor oxygen vacancy is significant for aluminum- and scandium-doped barium zirconate. In contrast, the yttrium-doped system shows 67% and 33% probabilities at 800 K for the dopant nearest and second nearest neighbor oxygen vacancies, respectively. The dopant nearest oxygen vacancy leaves the dopant polyhedral center charge exposed. The small size of the aluminum dopant allows oxygen ions to shift and partially screen the dopant charge. This coupled with strong hydrogen bonds increases proton trapping. For the larger scandium and yttrium ions, there is no significant oxygen ion rearrangement around the dopant with a nearest neighbor oxygen vacancy. Instead, the positive dopant charge exposed by the vacancy raises the energy of several dopant nearest neighbor proton sites decreasing trapping locally.

### ■ INTRODUCTION

Acceptor-doped barium zirconate is one of the most promising materials for stationary hydrogen fuel cells due to its high proton conductivity and structural stability. The lower valency dopant defect creates a proton trap. Some studies suggest that oxygen vacancies ( $V_O^{\bullet\bullet}$ ) near the acceptor dopant ( $D_{Zr}'$ ) help hinder proton trapping by enhancing proton conductivity. Further, some studies suggest that at high dopant concentrations (20% or more) that dopant clustering is common. Recent computational studies suggest that oxygen vacancies are more likely to form between acceptor dopant sites and the subsequent hydration places protons on nearest and second nearest oxygens. However, a follow up study using gradual hydration did not see a significant repulsion between the associated dopant/oxygen vacancy defects and protons to avert proton trapping at the dopant site.

The dopant is both a help and hindrance to proton conduction in barium zirconate. On the one hand, it is critical to the introduction of protons in the system. Doping at the B site with a lower valency ion introduces charge-compensating oxygen vacancies which are partially filled by oxygen from

water in humid environments. While an oxygen ion fills the vacancy, the liberated water protons move through the lattice of oxygen ions in the perovskite providing the key conducting species. Doping at higher concentrations increases the concentration of protons or conducting species. On the other hand, due to the lower valency of the dopant ions, there is increased electron density on oxygen vertices of the  $DO_6$  octahedra, creating a trap region for the protons which hinders their conduction. Our earlier work on barium zirconate 3,5,12,13 shows that  $AI'_{Zr}$  and  $Y'_{Zr}$  dopant defects shape the proton conduction landscape affecting proton conduction pathways, traps and key nexuses between trapped regions and proton conduction highways in significantly different ways.

Received: October 19, 2020 Revised: November 30, 2020 Published: December 11, 2020





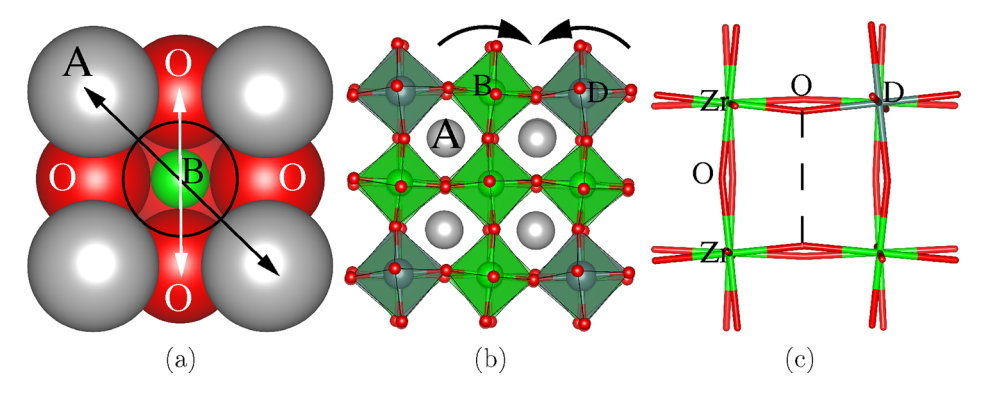


**Figure 1.** (a) Basic ABO<sub>3</sub> perovskite unit cell with a space filling model. Notice that the oxygen ions around the B ion form an octahedron. Four labeled oxygen ions are shown around the B ion, and there is also an oxygen below the B ion. The foremost oxygen has been made transparent for clarity. (b) Replicated perovskite unit cells in a polyhedral model highlighting octahedra around B ions and octahedra around dopant ions. The arrows above B and D octahedra indicate opposite direction tilting for adjacent octahedra which are connected by oxygen corners. (c) Stick model of the upper right cube in part b, highlighting a case where subsequent layers of the perovskite have an opposite tilting scheme. In part c, a pair of oxygen ions in each face approach each other while another pair separates. The dashed line highlights the closer oxygen ion pairs. The A ion has been omitted from the center of part c for clarity.

The basic perovskite ABO<sub>3</sub> unit structure shown in Figure 1a is altered by the dopant shaping the network of oxygen ions through which the proton conducts. As shown in Figure 1a, there are two key packings in the basic perovskite structure: the packing along the diagonal AOA and the packing along the body-centered line OBO. When the radii of the ions involved are ideal, the lattice size calculated from the diagonal packing and the body-centered line packing is the same. This is roughly the case for barium zirconate. When a larger dopant ion (D) is substituted at the B site, the new body-centered line ODO lengthens, increasing the lattice size and opening space for the oxygen ions in the AOA diagonal. The oxygen ions in the perovskite structure are octahedrally arranged around the B sites as shown in Figure 1b. Hence, the additional space by the oxygen ion octahedral vertex allows the octahedral tilting shown in Figure 1b. The tilting direction alternates on adjacent corner sharing octahedra. The tilting brings some oxygen ions closer together and others further apart leading to a greater diversity of oxygen types and hence a richer proton conduction energy landscape. 12,14 Octahedral distortions are categorized through the Glazer system: + and - refer to subsequent layers tilting in the same and opposite directions respectively, while 0 refers to no tilt occurring. 15 Figure 1c shows a Glazer distortion perpendicular to the surface normal. The Glazer distortion labels, for the surface normal to the three standard axes, and the degree of the distortion, which can be measured by the ZrOZr and ZrOD angle distributions, 14 describe the initial proton conduction landscape or network of oxygen ions.

While the basic network or landscape of oxygen ions through which the protons conduct is shaped by the dopant defects, further alteration can be made by other defects. and even changing the concentration of the defects. Since positively charged oxygen vacancies near the negatively charged dopant defect have the potential to decrease the attraction or trapping of a proton, it is important to determine how they further shape the proton conduction landscape and alter proton conduction pathways. As can be seen in parts b and c of Figures 1, there are a variety of types of oxygen sites and possible vacancy locations.

In this study, we explore the effect of an oxygen vacancy on the proton conduction landscape of barium zirconate with 12.5% dopant defects of increasingly larger size  $Al'_{Zr}$ ,  $Sc'_{Zr}$ , and

 $Y'_{Zr}$ . The effect of both physical lattice distortions and changing chemical composition are probed with the goal of understanding how the energy landscape changes near the oxygen vacancy for each of these systems. These systems represent a wide range of proton conductivity from the very slow proton conductor aluminum-doped barium zirconate to the fast proton conductor yttrium-doped barium zirconate.

#### METHODS

Finding the Optimum Tilting Structure in the Doped Barium Zirconate Systems. The 23 possible Glazer distortions for a 2 × 2 × 2 unit cell system of barium zirconate with one dopant defect  $(D_{Zr'})$  or a 12.5% doping level were generated. Each configuration was optimized using the conjugate gradient method allowing both ions and cell size to vary. The convergence stopping criterion required forces to be less than 0.01 eV/Å. The energy optimized was the density functional theory (DFT) energy with the PBE functional in the Vienna ab initio simulation package (VASP). A plane wave basis set generated from a 2 × 2 × 2 k-point mesh was used with energy cutoff of 600 eV. A background charge compensating cloud was used.

Finding the Effect of Oxygen Vacancies on the Basic Doped Perovskite Structures and Possible Oxygen Vacancy Conduction. In a  $2 \times 2 \times 2$  unit cell perovskite system with one dopant ion, there are 24 possible oxygen ion locations but only three of these are distinct by symmetry. As shown in Figure 2, the three types of oxygen ion sites at which a vacancy could be introduced are nearest (I), second nearest (II), and third nearest (III) neighbors to a dopant defect. While the specific dopant in Figure 2 is yttrium, the geometrical oxygen ion site distribution is the same although with decreased octahedral tilting when doping with the smaller ions.

The combination of two defects, a proton and an oxygen vacancy, in a  $2 \times 2 \times 2$  unit cell system can disrupt tilting patterns through the entire small periodic system. To avoid periodic small system size issues, a simulation box of  $4 \times 4 \times 4$  unit cells was used when introducing vacancies and protons, rather than the  $2 \times 2 \times 2$  unit cells used to find the best Glazer tilting arrangement. The large system is created by replicating the optimum Glazer tilting arrangement twice in each

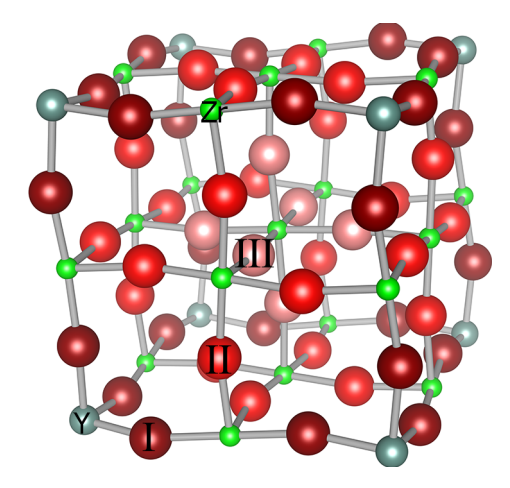


**Figure 2.** General structure of a 12.5% yttrium-doped  $2 \times 2 \times 2$  unit cell barium zirconate system is shown. The oxygen sites nearest (I), second nearest (II), and third nearest (III) neighbors to the yttrium are shown in decreasing shading of red, respectively. Zirconium ions are shown in green; yttrium is shown in teal. Barium ions have been omitted for clarity.

direction. A single gamma point was used to generate the plane wave basis set for the  $4 \times 4 \times 4$  unit cell systems. The same electronic structure method and ionic conjugate gradient optimization is used as described for the Glazer distortions. Testing on selected structures showed that for the larger system, relative energies found with a single gamma point were similar to those found using the  $2 \times 2 \times 2$  *k*-point mesh. The nudged elastic band (NEB) method followed by the climbing nudge elastic band (cNEB) method  $^{22-24}$  with two images, spring constants of 5.0 eV/Ų, and force optimizers was used to find activation barriers for oxygen vacancy motion with force convergence criteria set to 0.02 eV/Å.

Finding the Effect of an Oxygen Vacancy on Proton Binding Sites and Proton Transport. Proton binding sites can be divided into eight distinct categories which are highlighted by a different color in Figure 3. Protons in the same categories have the same distance distributions with other ions. As shown in Figure 2, oxygen ions are nearest (I), second nearest (II), or third nearest (III) from the dopant. Further, as seen in Figure 1c, every face has a closer pair of oxygen ions and a farther pair. The  $H_I^{Close}$  protons in Figure 3 are on dopant nearest neighbor oxygen ions and hence are labeled with an I subscript. The Close superscript denotes that the oxygen ion in the hydroxyl is part of a close oxygen ion pair like the pair connected by a dashed line in Figure 1c. The  $H_I^{\it Far}$ protons are also on a dopant nearest neighbor oxygen ion. However, the oxygen ion binding the proton is part of a farther apart oxygen ion pair. Using the same strategy, protons on the type III oxygen ions (third nearest to the dopant ions) are called  $H_{III}^{Close}$  and  $H_{III}^{Far}$ . The  $H_{IID}^{Close}$  and  $H_{IID}^{Far}$  protons are protons on dopant second nearest neighbor oxygen ions with hydroxyls on planes that contain the dopant. Respectively, the  $H_{IIND}^{Close}$  and  $H_{\text{IIND}}^{Far}$  protons are on dopant second nearest neighbor oxygen ions with hydroxyls on planes that do not contain the dopant. The optimized structures and energies for each type of proton binding site were found in the system without an oxygen vacancy and with an oxygen vacancy at many distances away from the vacancy. Both cases use the lattice size and shape optimized including the oxygen vacancy.

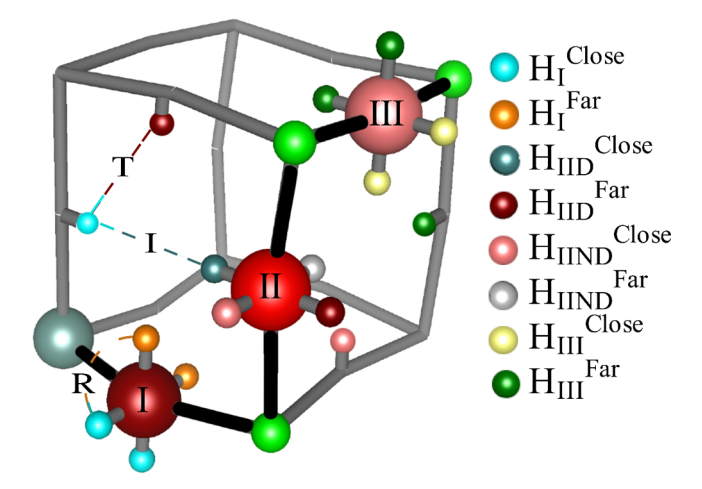


Figure 3. There are eight distinct categories of protons, highlighted by different colors in the legend. The proton site categories are each labeled with a subscript denoting attached oxygen ion type and hydroxyl planar environment and a superscript indicating whether the oxygen ion in the hydroxyl is part of the close oxygen ion pair connected with a dashed line in Figure 1c. For example, the  $H_I^{Close}$  protons are on dopant nearest neighbor oxygen ions and are hence labeled with I in the subscript. The *Close* superscript label notes that the oxygen ion that the proton is on is part of a closer oxygen ion pair. Protons on type II oxygen ions where the hydroxyl is in a plane including the dopant include a D in the subscript label where as those on a plane not including the dopant use an ND in the subscript label. Protons can also move between sites by rotation (R), intraoctahedral transfer (T), or interoctahedral transfer (I). One example of each type of motion is depicted and labeled.

Protons can move between sites by rotation (R), intraoctahedral transfer (T), or interoctahedral transfer (I). Rotation moves a proton between sites on the same oxygen ion, for instance from  $H_{I}^{\it Close}$  to  $H_{I}^{\it Far}$  as indicated by a blue/ orange curved line labeled R in Figure 3. Intraoctahedral transfer refers to a proton transfer movement between oxygen ions on the same octahedron, for example from  $H_I^{Close}$  to  $H_{IID}^{Far}$ as indicated by the blue/brown solid straight line labeled as T. Note that the cube in Figure 3 has octahedral centers at each corner. Inter octahedral transfer refers to a proton transfer between oxygen ions on different octahedra such as from  $H_I^{Close}$ to  $H_{IID}^{Close}$  as indicated by the blue/teal straight line labeled I. There are 10 distinct types of rotations, eight distinct types of intraoctahedral transfer, and two types of interoctahedral transfer. Transition states for all these motions were calculated in the absence of an oxygen vacancy, and the ones closest to the vacancy were calculated in the presence of the vacancy. Since the same lattice size and shape is used with and without the vacancy, it is expected that the transitions in the absence of the vacancy are similar to those far from the vacancy. The same approaches as for oxygen vacancy moves namely a sequence of NEB and cNEB methods<sup>22–24</sup> were used. When two images did not yield convergence, four images were used.

# RESULTS

Lattice Size and Octahedral Tilting Increase with Dopant Ionic Size. The lowest energy Glazer distortion pattern<sup>15</sup> found for each system was (-,-,-) as seen in our earlier studies of the yttrium-doped system.<sup>12</sup> The distortions are very slight in the aluminum case. As a result, our earlier

study<sup>3</sup> noted that dopant layers were nearly undistorted. This study which uses the stricter criteria of force convergence to  $0.01 \, \mathrm{eV/\mathring{A}}$  rather than the default energy convergence finds the same energy for both our earlier study best structure<sup>3</sup> and the (-,-,-) structure. To make comparison between the three dopant systems simpler, the (-,-,-) distortion is used for all three systems. In the yttrium-doped system, the (0,0,0) no tilt pattern is  $0.10 \, \mathrm{eV}$  higher in energy than the (-,-,-) pattern. In contrast, in aluminum- and scandium-doped systems, the corresponding energy difference is less than  $0.02 \, \mathrm{eV}$ . However, given that there are other tilting pattern minima within  $0.02 \, \mathrm{eV}$  of energy in all systems, the key result is that tilting increases as the dopant size increases. As shown in Table 1, the lattice size

Table 1. Shannon Ionic Radii, Lattice Size Assuming Close Packing with Shannon Ionic Radii, Lowest Energy Lattice Size Found Using DFT in This Study, and Experimental Lattice Constants for Systems with Each of the Dopant Defects Considered<sup>a</sup>

defect	ion radius (Å)	Shannon calculated lattice constants (Å)	average optimized lattice constants (Å)	experimental lattice constants (Å)
$\mathrm{Al}_{Zr}{}'$	0.535	4.20	4.24	. ,
$\mathrm{Zr}_{Zr}$	0.72	4.25	4.25	$4.19^{25}$
$\operatorname{Sc}_{Zr}{}'$	0.745	4.25	4.26	4.20 <sup>26</sup>
$\mathbf{Y}_{Zr}{}'$	0.90	4.29	4.29	$a = 4.23,$ $c = 4.21^{2}$
				$c = 4.21^{2}$

"Optimized lattice constants for the undoped system can vary greatly from 4.10 to 4.40 Å with exchange correlation functional and pseudopotential choice.<sup>27</sup> The variation found with dopant in this system is smaller than the variation found with functional choice.

increases as the dopant ion radius increases, giving the same trend as experiment.<sup>25,26</sup> The yttrium-doped average lattice size is in agreement with other studies that allow full simulation box relaxation<sup>14</sup> but is slightly larger than in studies maintaining cubic symmetry in the simulation box.<sup>12</sup>

Octahedral tilting increases as dopant ionic size increases. As shown in Figure 4, the lighter gray solid rectangle Zr–O–Al angle distribution shifts closer to 180° (less tilting) than the corresponding gray solid rectangle Zr–O–Zr angle distribution, while the lighter gray rectangle Zr–O–Sc angle distribution remains within the gray solid rectangle Zr–O–Zr angle distribution. Finally, the lighter gray rectangle Zr–O–Y angle distribution shifts away from 180° relative to the gray solid rectangle Zr–O–Zr angle distribution. Figure 5 highlights a section of the simulation box to emphasize the visual effect of the tilting. As tilting increases, one pair of oxygen ions in each face come closer together while another gets further apart. The effect is most pronounced in the yttrium system.

Oxygen Vacancy Site Energies Dependence on both Dopant Proximity and Local Octahedral Tilting Flexibility. The presence of a vacancy at a dopant nearest (I), second nearest (II), and third nearest (III) neighbor oxygen site alters local octahedral tilting broadening the ZrOX distributions shown in Figure 4. While the broadening is similar for all types of vacancies, the relative energies between systems with different types of vacancies are significantly different. In all dopant systems, the lowest energy oxygen vacancy occurs at a dopant nearest neighbor oxygen site which is expected as the positive vacancy defect  $(V_{O}^{\bullet})$  and negative dopant defect  $(D_{Zr})$  attract. Based on distance alone, we would expect that the energy of the vacancy at increasing

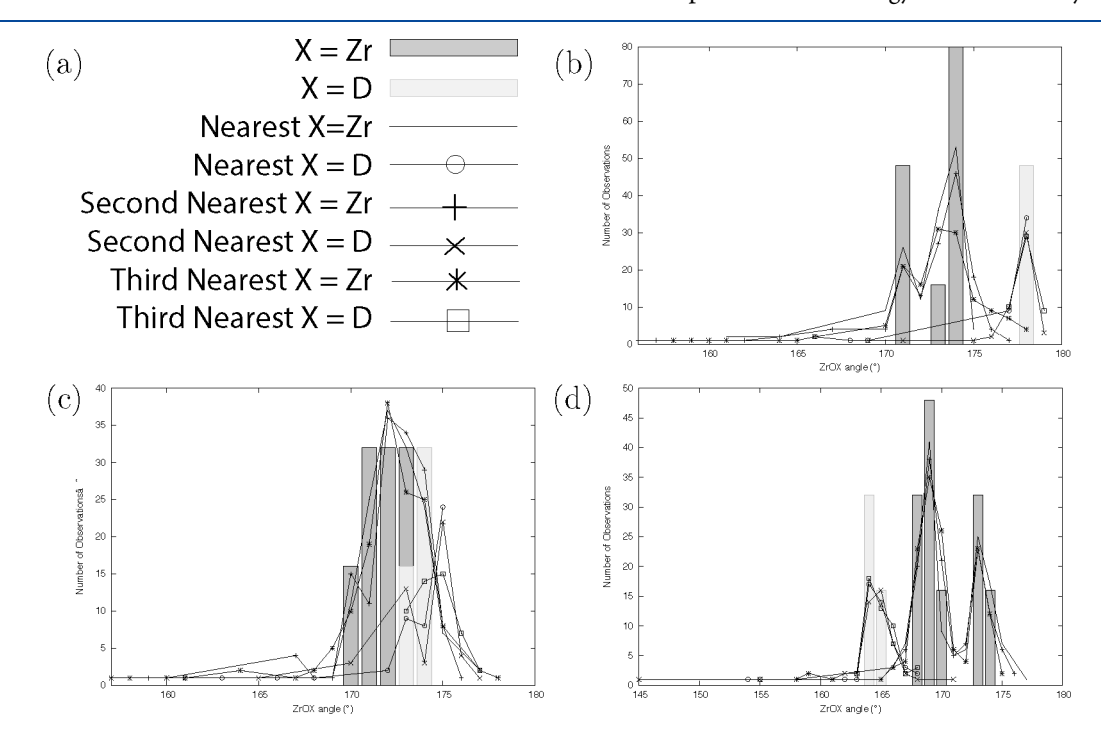
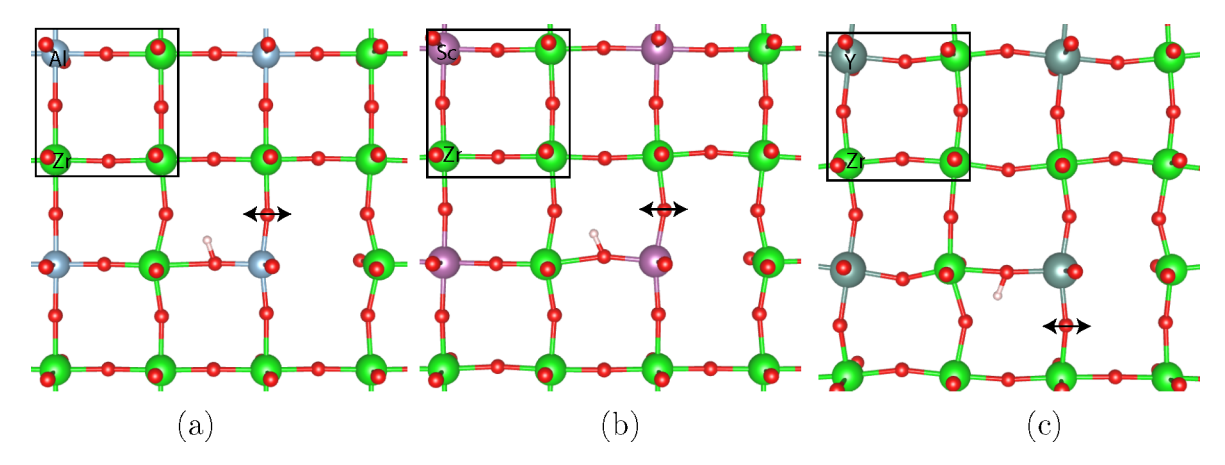


Figure 4. (a) Legend for angle distributions. The Zr-O-X angle distributions are shown for the (b) Al-, (c) Sc-, and (d) Y-doped systems as solid gray rectangles when X = Zr and lighter gray rectangles when X = D where D is the dopant. When there is a dopant nearest neighbor oxygen vacancy, a solid line and a line with open circles mark the Zr-O-Zr and Zr-O-D distributions. When there is an dopant second nearest neighbor oxygen vacancy, Zr-O-Zr and Zr-O-D angle distributions are shown with lines with plus and times symbols, respectively. Finally, Zr-O-Zr and Zr-O-D angle distributions when there is a dopant third nearest neighbors oxygen vacancy are highlighted with star and square symbols on lines. As the dopant size increases, there is a greater shift away from the  $180^{\circ}$  for Zr-O-D angles relative to Zr-O-Zr angles. When the vacancy is introduced, the distributions broaden.



**Figure 5.** Upper left square of the Al (a), Sc (b), and Y(c) systems, respectively, visually highlights increased tilting with increasing dopant ion size far from an oxygen vacancy. As tilting increases, a pair of oxygen ions gets closer together while the other pair gets further apart. The double-headed arrow in these high energy minima highlights the opposing pulls on an oxygen ion toward the positive proton and oxygen vacancy defects. For clarity, only a section of the simulation box is shown.

Table 2. Relative Energies and Probabilities at 800 K of Oxygen Vacancies at Dopant Nearest (I), Second Nearest (II), and Third Nearest (III) Neighbor Oxygen Sites

	Al		Sc		Y	
	energy (eV)	probability at 800 K	energy (eV)	probability at 800 K	energy (eV)	probability at 800 K
$VI^{\bullet \bullet}$	0.00	1.00	0.00	0.98	0.00	0.67
VII••	0.98	0.00	0.43	0.00	0.05	0.33
VIII••	0.53	0.00	0.29	0.02	0.41	0.00

separation from the dopant would increase. However, the remaining energy pattern shown in Table 2 is a compromise between  $V_O^{\bullet \bullet} - D_{Zr}'$  interactions,  $V_O^{\bullet \bullet}$  -nearby  $O_O$  pair interactions, and strain caused by stretching Zr-O bonds to bring oxygen ions closer to the vacancy when octahedral tilting is not possible. Figure 2 shows that type II oxygen ions and hence vacancies at type II sites  $(V_{II}^{\bullet \bullet})$  are in dopant-containing planes. As seen in Figure 4, ZrOD angles are closer to 180° indicating decreased octahedral tilting in aluminum and scandium systems than in yttrium systems. When octahedral tilting can not be used to bring two nearby negative oxygen ions closer to the positive vacancy defect, the ZrO and DO bonds must be stretched with a higher energy cost. As Table 2 shows, the energy of a vacancy at a type II oxygen is indeed high in Al and Sc systems but low in the yttrium system where octahedral tilting flexibility in dopant planes can bring oxygen ions closer to the vacancy. Figure 2 shows that type III oxygen ions and hence  $V_{III}^{\bullet \bullet}$  are in planes without dopant ions. Since the ZrOZr broadened angle distributions shown in Figure 4 show some ZrOZr angles in the 165-175° region in all systems, oxygen ions can approach a  $V_{\it III}^{\bullet \bullet}$  through tilting and less stretching of bonds is needed than in the dopant planes of Sc and Al systems. At the same time, the type III vacancy site is further away from the dopant defect, leading to a higher energy than the vacancy closest to the dopant defect. Since perovskite proton conductivity is measured in the wide range of 500-1500 K<sup>1</sup> and yttrium-doped barium zirconate shows high conductivity at 750 K, <sup>28,29</sup> the Boltzmann probabilities for each type of vacancy at 800 K for each doped system are shown in Table 2. For the aluminum and scandium systems, nearest neighbor oxygen sites are the most likely position for an oxygen vacancy. However, in the yttrium system, finding the vacancy at a nearest neighbor oxygen site is only about twice as

likely as finding it at a second nearest neighbor oxygen site. Transition energy barriers for all possible vacancy moves are shown in Table 3. In aluminum and scandium systems, there

Table 3. Forward  $(E_f)$  and Backward  $(E_b)$  Energies Barriers for Each Type of Oxygen Vacancy Transition in  $eV^a$ 

	Al		Sc		Y	
$V_{O}^{\bullet \bullet}$ transition	$E_f$ (eV)	$E_b$ (eV)	$E_f$ (eV)	$E_b$ (eV)	$E_f$ (eV)	$E_b$ (eV)
I to I	0.02	0.02	0.01	0.01	0.02	0.02
I to II	1.05	0.07	0.72	0.29	0.05	0.00
II to III	0.01	0.47	0.48	0.62	0.36	0.00

<sup>a</sup>I, II, and III refer to having the vacancy at a first, second, or third nearest neighbor oxygen site from the dopant.

are low barriers for oxygen vacancy motion between type I oxygen ion sites and high barriers to move away from the sites closest to the dopant. However, in the yttrium system, barriers are also low for oxygen vacancy moves from type I to type II oxygen sites and hence to second nearest neighbor sites away from the dopant. Dynamic simulations of oxygen vacancies would need to include intraoctahedral vacancy moves on doped octahedra in all systems and add the interoctahedral vacancy move from an oxygen site nearest to the dopant to a second nearest site.

Type I Oxygen Vacancies Significantly Altering Proton Binding Site Energies and Conduction Barriers. In the absence of an oxygen vacancy, each proton type defined in Figure 3 can exhibit hydroxyl rotation to facilitate hydrogen bonding leading to a slight energy variation (less than 0.04 eV). Figures 6, 7, and 8 reveal that relative energies of each proton type as a function of  $V_0^{\bullet\bullet} - D_{Zr}'$  distance for D = Al, Sc, and Y dopant defects, respectively, are altered significantly up through a distance of 6 Å away from the vacancy. Beyond 6 Å,

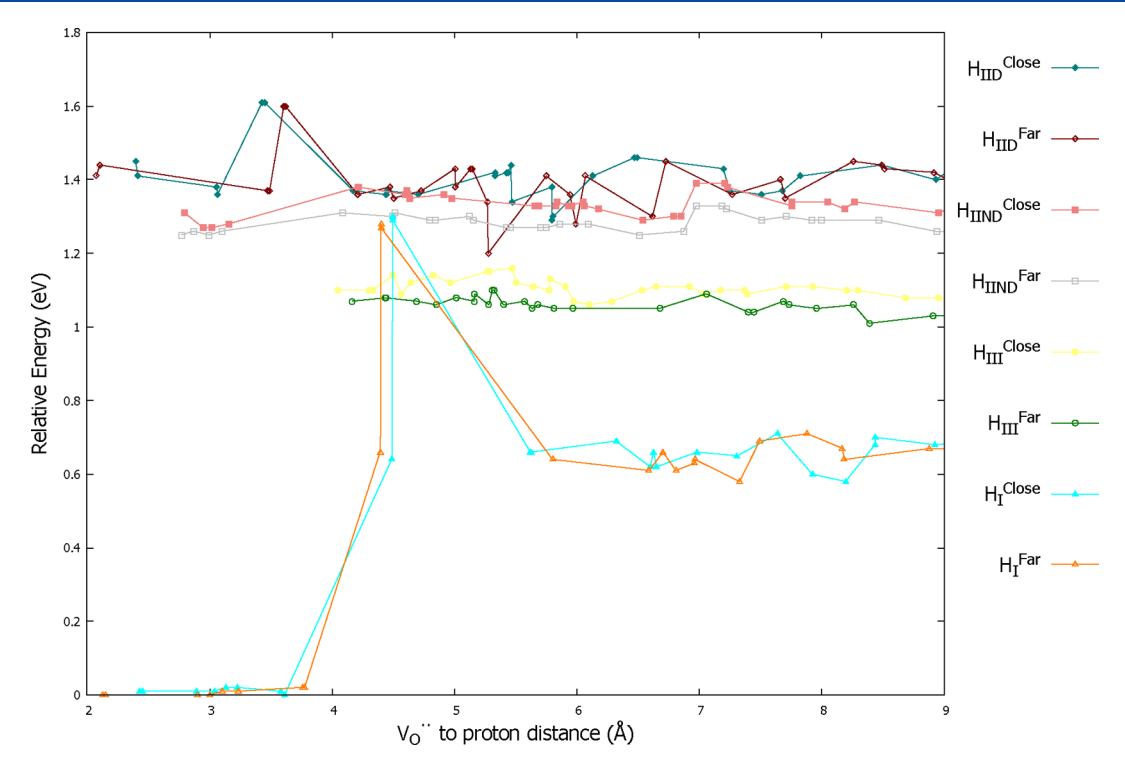


Figure 6. Relative energy as a function of proton distance from the oxygen vacancy for the aluminum-doped system. The legend order mirrors the relative energies at a large distance away from the vacancy.

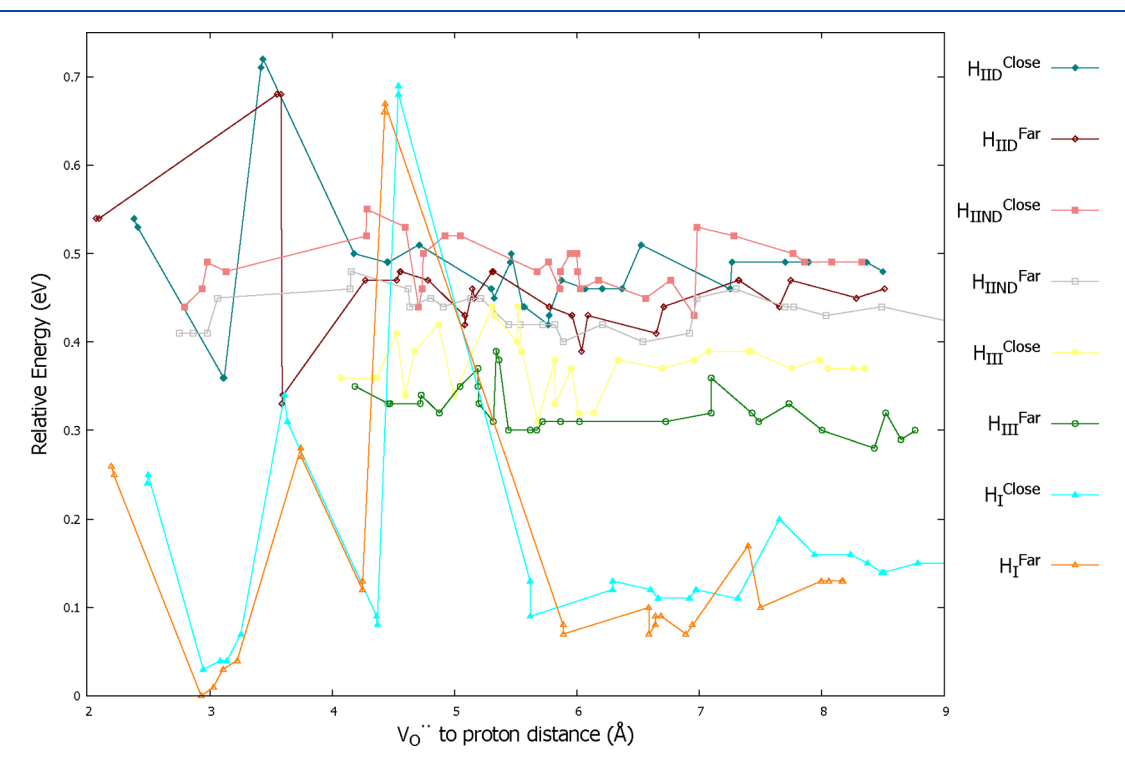


Figure 7. Relative energy as a function of proton distance from the oxygen vacancy for the scandium-doped system. The legend order mirrors the relative energies at a large distance away from the vacancy.

the relative energy pattern is the same as the pattern in the absence of the vacancy with the same lattice size.

The relative energy gaps between the different proton sites at the largest distances away from oxygen vacancy are also the same as the gaps in the same lattice systems in the absence of the vacancy. The pattern far away from the vacancy is also consistent with earlier work in aluminum- and yttrium-doped barium zirconate systems with higher proton concentration even though the aluminum system used a different Glazer distortion. In aluminum and scandium systems far away from the vacancy, the site energies rise from proton sites on type I to III to II oxygen ions. This is the same energy rise pattern as we saw for oxygen vacancies in Table 4. The tilting possible in type III oxygen planes facilitates hydrogen bond

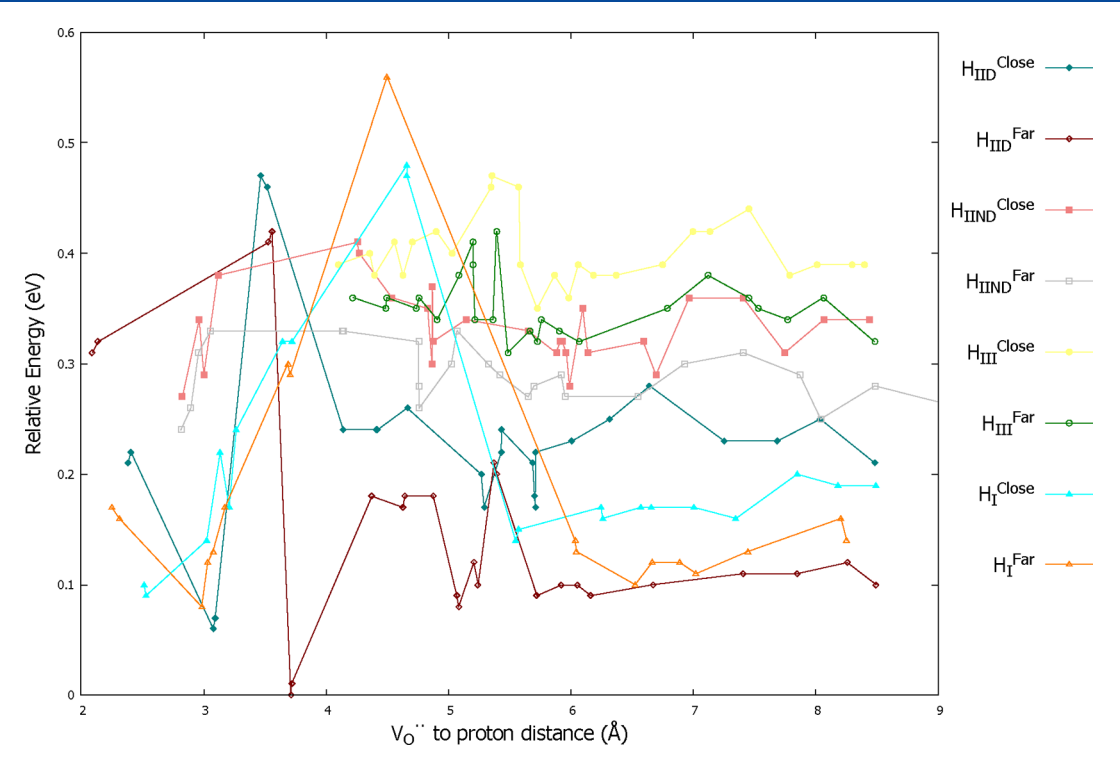


Figure 8. Relative energy as a function of proton distance from the oxygen vacancy for the yttrium-doped system.

Table 4. Most Critical Barriers to Proton Conduction (in eV) for Aluminum-, Scandium-, and Yttrium-Doped Systems Closest to the Vacancy and in the Absence of the Vacancy in Parentheses<sup>a</sup>

	Al	Sc	Y
$\mathrm{T}(H_{I}^{Far},H_{IID}^{Close})$	1.40* (0.97)	0.10 (0.53)	0.00 (0.14)
$\mathrm{T}(H_{IID}^{Far},H_{IID}^{Close})$	0.04 (0.01)	0.08 (0.07)	0.00 (0.01)
$\mathrm{T}(H_{IID}^{\mathit{Close}},H_{IID}^{\mathit{Far}})$	0.00 (0.00)	0.09 (0.03)	0.00 (0.01)
$\mathrm{T}(H_{I}^{ extit{Close}},H_{I\hspace{-0.1cm}I\hspace{-0.1cm}I\hspace{-0.1cm}D}^{ extit{Far}})$	1.36* (0.75)	0.10 (0.48)	0.00 (0.01)
$R(H_{IID}^{Close}, H_{IIND}^{Close})$	0.07 (0.01)	0.00 (0.02)	0.16 (0.09)
$\mathrm{R}(H_{IID}^{Close},H_{IIND}^{Far})$	0.10 (0.01)	0.00 (0.02)	0.10 (0.04)
$\mathrm{R}(H_{IID}^{Far},H_{IIND}^{Close})$	0.01 (0.01)	0.01 (0.04)	0.00 (0.25)
$\mathrm{R}(H_{IID}^{Far},H_{IIND}^{Far})$	0.00 (0.08)	0.01 (0.01)	0.00 (0.24)

"A \* indicates a transition starting from the trigonal bipyramidal distortion shown in the end points of Figure 9.

formation as it aids in bringing oxygen ions closer to the oxygen vacancy. However, in the yttrium system, which has enhanced tilting in dopant planes, the  $H_{IID}^{Close}$  site is 0.04 eV lower in energy than the  $H_{I}^{Far}$  site far from the vacancy or in the absence of the vacancy in the same lattice size and shape simulation box. Furthermore, type III proton sites have the highest energy in the yttrium system. Getting away from a proton site on a dopant nearest neighbor oxygen or from the dopant trap requires going through a site on a second nearest neighbor oxygen ion. Since the proton sites on all second nearest neighbor oxygen ions have highest energy far from the vacancy in the aluminum and scandium systems, proton conduction requires a larger change in energy in these systems than in the yttrium system.

When a dopant nearest neighbor oxygen vacancy is introduced, many protons within each site category in Figure 3 have different distances to the oxygen vacancy, and hence, protons in each site category no longer have the same energy. Figures 6, 7, and 8 show the relative energies of proton binding sites in each color category as a function of their distance from

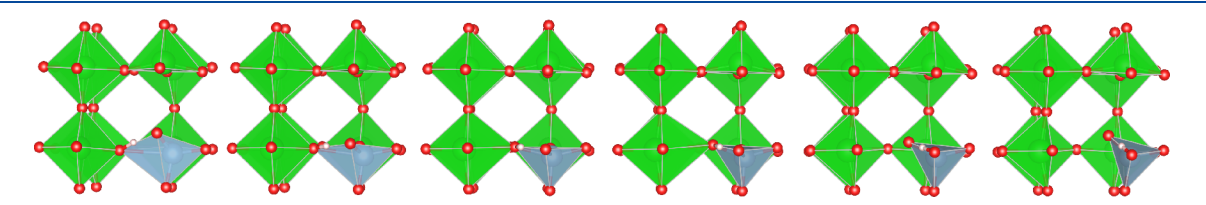


Figure 9. Lowest energy configurations with a proton on a nearest neighbor oxygen to the vacancy rearrange oxygen ions around the aluminum ion into an elongated trigonal bipyramidal structure. This trigonal bipyramidal structure is seen horizontally in the first image  $(H_I^{Far,*})$  optimized from the  $H_I^{Far}$  structure and going into the page in the last image  $(H_I^{Close,*})$  optimized from the  $H_I^{Close}$  structure. This rearrangement from square pyramidal (octahedron with one vacancy) to trigonal bipyramid leads to the drastic energy lowering shown in Figure 6 close to the oxygen vacancy. The intermediate images show that the proton transfer between these two images occurs after first rearranging the trigonal bipyramid to a square pyramid. Finally, relaxation to a differently oriented trigonal bipyramid occurs.

an oxygen vacancy on an oxygen nearest neighbor site to the dopant for aluminum, scandium, and yttrium, respectively. All proton binding sites near the vacancy up to 6 Å are included. Beyond this distance, only about one in three protons are included since at this point the energies fluctuate less. While the long-range energies for each type of proton plateau, there are significant fluctuations at distances closer to the vacancy. At these close distances, the proton defect and the oxygen vacancy defect can be accommodated by local distortions involving the same nearby oxygen ions. The structures for the highest energy  $H_I$  site points in Figures 6, 7, and 8 are shown in parts a-c of Figure 5, respectively. A double-headed arrow highlights the competing ways an oxygen ion between the two positively charged defects can accommodate the defects. Neither octahedral tilting nor deformation can satisfy both pulls simultaneously, leading to a high energy structure. In low energy configurations, local distortions around the proton reinforce distortions around the vacancy.

In the aluminum system, there is a significant energy lowering of the  $H_I^{Close}$  and  $H_I^{Far}$  sites caused by oxygen ion rearrangement around the aluminum from a square pyramid (octahedron with one vacancy) to a trigonal bipyramid. This structure is shown in Figure 9 in the first and last images. Furthermore, in all systems, there are large fluctuations in energy of the proton binding sites on dopant nearest neighbor oxygen ions when the proton is within 6 Å of the oxygen vacancy. As can be seen in Figure 2, proton motion in planes containing the dopant requires moves through type I and II oxygen ions for long-range conduction. Conduction in planes without the dopant requires proton moves through type II and III oxygen ions. Getting away from a dopant nearest neighbor oxygen (nearly the lowest energy site in all systems) requires going through a second nearest neighbor oxygen ion. This suggests that the aluminum system with its over 1.2 eV gap between the lowest energy proton sites on type I and II oxygen ions will be the poorest proton conductor of the three. The scandium system has a smaller energy gap between the lowest energy proton sites on type I and II oxygen ions, suggesting possible conduction. Finally, the yttrium system has the smallest gap between proton sites on oxygen ions adjacent to the dopant and protons on second nearest oxygen ions (brown) indicating that conduction may be very favorable. Overall, the fact that the energy range between binding sites in the largest dopant is the smallest suggests a greater likelihood of faster conduction in that system.

Earlier studies  $^{3,5,16}_{I}$  showed that proton conduction in the aluminum system occurred through periodic escapes from the dopant trap to planes without the dopant where the proton could travel quickly through a fast conduction pathway before getting trapped again at another dopant site, while proton conduction in the yttrium system kept the proton near the trap. Effectively, proton conduction in the aluminum system moved through proton binding sites on type I, II, and III oxygen ions, while conduction in the yttrium system moved through only proton sites on type I and II oxygen ions. Pathway searches  $^{13}_{I}$  show long-range pathways with intraoctahedral transfers from  $H_{IID}^{Far}$  and  $H_{IIND}^{Far}$  to  $H_{IIND}^{Close}$  as well as rotations from  $H_{IID}^{Close}$  to  $H_{IIND}^{Close}$  and  $H_{IIND}^{Far}$  as one way to escape the dopant in one direction. To escape the dopant in the perpendicular direction, intraoctahedral transfers from  $H_{IID}^{Far}$  to  $H_{IID}^{Close}$  are followed by rotations from  $H_{IID}^{Far}$  to  $H_{IIND}^{Close}$  and  $H_{IID}^{Close}$  are followed by rotations from  $H_{IID}^{Far}$  to  $H_{IID}^{Close}$  and

 $H_{IIND}^{Far}$  were seen. Review of Figure 3 shows that the first set of paths feature moves to and from the teal  $H_{IID}^{Close}$  while the second set of paths feature moves to and from the maroon  $H_{IID}^{Far}$  as critical moves to advance a proton from the environment near one dopant to the environment near the next unit's dopant ion in one direction. For the Y system, these critical, lowest-energy sites are indicated by the orange  $H_{I}^{Far}$  and maroon  $H_{IID}^{Far}$  markers. For the aluminum system, however, the critical transitions start at the lowest energy sites indicated by blue  $H_{I}^{Close}$  and orange  $H_{I}^{Close}$  and transfer the proton to maroon  $H_{IID}^{Far}$  and teal  $H_{IID}^{Close}$ . To compare aluminum, scandium, and yttrium systems, barriers for all these moves in the presence and absence of an vacancy are compared in Table 4.

Due to the small aluminum size, the oxygen ions can rearrange its neighborhood to partially delocalize the oxygen vacancy as seen in the end points of Figure 9. Transfers between proton sites on different oxygen ions in resulting trigonal bipyramidal structures such as that shown in Figure 9 still occur and involve polyhedral rearrangements. Rotations between proton sites on the same oxygen ion in trigonal bipyramidal structures can involve hydrogen bonding changes as the hydroxyl group changes orientation to point to a different nearby oxygen ion. These transitions were not explored in detail as the trigonal bipyramidal rearrangement in the aluminum system leads to a significant rise from 0.75 to 1.36 eV in one of the typical barriers to long-range conduction  $(T(H_{I}^{Close}, H_{IID}^{Far}))$  namely the lowest barrier to escape the dopant trap shown in Table 4. The other transfer barrier to escape the dopant trap in aluminum-doped systems (T( $H_I^{Far}$ ,  $H_{\rm IID}^{\rm Close}$ )) has increased from 0.97 to 1.40 eV. In contrast, the corresponding typically lowest energy barrier to long-range conduction  $(T(H_I^{Close}, H_{IID}^{Far}))$  for scandium has gone from 0.48 to 0.10 eV close to the vacancy. The other transfer barrier to escape the dopant trap in the scandium-doped system (T( $H_I^{Far}$ ,  $H_{IID}^{Close}$ )) has decreased from 0.53 to 0.10 eV making both transfer escapes to the dopant trap smaller and destabilizing the original trap. The new lowest energy site is not adjacent to the vacancy but about 2.9 Å away as shown in Figure 7. It is possible that the limiting barrier has simply shifted in distance away from the vacancy.

The yttrium system experiences similar destabilization near the trap. The lowest and second lowest energy proton sites in the yttrium system are  $H_{IID}^{Far}$  and  $H_{I}^{Far}$ , respectively. The lowest energy path starting at the lowest energy site moves the proton away from the environment of one dopant to the next dopant through transfers to  $H_{IID}^{Close}$  and rotations from this point in the absence of the vacancy or far from it. The path is  $(T(H_{IID}^{Far}),$  $H_{IID}^{Close}$ ) followed by  $R(H_{IID}^{Close}, H_{IIND}^{Far})$ , and it has a limiting rotational barrier of 0.04 eV. If the path had started at  $H_I^{Far}$ , the limiting barrier would have been the intraoctahedral  $T(H_{IID}^{Far}, H_{IID}^{Close})$  0.14 eV barrier. The same paths in the presence of a vacancy have a rotational limiting barrier of 0.10 eV. Considering the pathways transferring to  $H_{IID}^{Far}$  and rotating away from the same point instead leads to the lowest energy paths with a rotational  $R(H_{IID}^{Far}, H_{IIND}^{Far})$  barrier of 0.24 eV in the absence of the oxygen vacancy and 0.00 eV in the presence of the vacancy. So, the fastest conduction path near the vacancy changes in the yttrium-doped system and overall the barrier lowers near the vacancy. As with the scandiumdoped system, a more complete study of barriers at many distances away from the oxygen vacancy is needed as the vacancy moves the lowest energy proton binding site to about 3.7 Å away from the vacancy.

Note that the lowest energy limiting barrier in the absence of the vacancy in the yttrium system is significantly lower than the 0.30 eV found in our earlier work. Furthermore, the type of move for the limiting barrier is also different. Our earlier calculations on smaller systems used a smaller cubic lattice size of 4.26 Å rather than allowing the system to deform to a 4.29 Å lattice size as was done in this study and had a different energy cutoff for the plane waves generated. These changes inverted the energy order of the lowest two energy sites and affected relative barriers for different rotations and transfers. This suggests that the lowest energy path and limiting barriers to long-range proton conduction depend significantly on the lattice size.

# DISCUSSION AND CONCLUSIONS

Lattice size and octahedral tilting increase with dopant ionic size in the barium zirconate backbone. Zr-O-D and Zr-O-Zr angle distributions show an increasing shift away from 180° in Zr-O-D angle relative to Zr-O-Zr angles as dopant ion size increases. Optimizations including an oxygen vacancy and/or a proton defect showed local changes from this tilting pattern near defects but retained the pattern at a distance. While DFT geometry optimizations find zero temperature structures, recent DFT molecular dynamics simulations at proton conduction temperatures (500-1000 K) retain significant octahedral tilting. 30 Torayev et al. note distinct "bent outward" and "bent inward" sites which correspond to our  $H_I^{Close}$  and  $H_I^{Far}$  sites. The molecular dynamics simulations  $^{30}$  reveal only intraoctahedral moves from  $H_{I}^{Close}$ to  $H_{IID}^{Far}$  and not from  $H_{I}^{Far}$  to  $H_{IID}^{Close}$ , the higher energy intraoctahedral move in the study, suggesting that tilting is critical to proton conduction mechanism in the absence of an oxygen vacancy.

Introducing a vacancy at oxygen sites nearest (I), second nearest (II), and third nearest (III) from the dopant broadens the angle distributions and leads to a small contraction in lattice size in agreement with Jedvik et al.<sup>31</sup> The energies of oxygen vacancies at these different sites reflect a competition between  $V_O^{\bullet\bullet}$  – $D_{Zr'}$  interactions,  $V_O^{\bullet\bullet}$  –nearby  $O_O$  interactions, and strain caused by stretching Zr-O bonds to bring oxygen ions closer to the vacancy when octahedral tilting is not possible. The vacancy closest to the dopant defect is always the lowest energy configuration. However, a vacancy at a second nearest oxygen site is in the dopant plane and has higher energy than a vacancy at the third nearest site in the aluminum- and scandium-doped systems. In these cases, Zr-O-D angles are closer to linear and do not allow octahedral tilting in dopant planes to bring nearby oxygen ions closer to the vacancy and instead force an option with higher energy cost namely Zr-O and D-O bond stretching. In contrast, dopant third nearest oxygen vacancies are not affected as these are on planes without dopant ions and Zr-O-Zr angle distributions remain roughly the same for all dopant systems. The tilting flexibility in the yttrium-doped system results in low energy oxygen vacancies at both the dopant nearest and second nearest oxygen sites. Activation barriers found for oxygen

vacancy conduction show that intraoctahedral oxygen vacancy moves between sites adjacent to the dopant are important in all systems. In the more flexible yttrium system, interoctahedral oxygen vacancy moves between dopant nearest and second nearest vacancy sites exhibit low barriers. However, in the aluminum and scandium systems, barriers to interoctahedral oxygen ion transfer were higher than intraoctahedral ones in agreement with a study by Hermet et al.<sup>32</sup> on oxide ion and proton transport in Gd-doped barium cerate.

The octahedral tilting flexibility in the yttrium-doped system also allows tilting to move oxygen ions closer to hydroxyls facilitating hydrogen bonding in planes including the dopant ions. This lowers the energy of the  $H_{\rm IID}^{\rm Far}$  proton site in agreement with recent work 30 showing that angle bending or octahedral tilting has a clear correlation with energy. Since long-range proton conduction requires escaping the dopant trap, a lower energy proton site on a type II oxygen is critical. In contrast, in the Al-doped system, a structural rearrangement from a square pyramid (octahedron with a vacancy) to a trigonal bipyramid leads to a significant lowering of energy for protons on the nearest oxygen site  $H_I^{Close}$  and  $H_I^{Far}$  and creates a larger dopant trap increasing the energy gap between protons on type I and type II oxygen ions. This square pyramid to trigonal bipyramid rearrangement around a small ion has been identified in our earlier double perovskite studies.<sup>33</sup> In general, the energy gap between protons on type II oxygen ions and those on type I oxygen ions gets smaller as the dopant size increases both far from the vacancy and close to the vacancy.

Earlier work 5,13,16 highlighted key transitions for aluminum trap escape and the more common barriers to long-range conduction in the yttrium system. The key transitions to escape the aluminum trap show increased barriers due to stabilization of the oxygen vacancy through a distortion from a square pyramid structure to a trigonal bipyramid. In contrast, the larger scandium and yttrium radii do not allow for this distortion and experience a lowering of the common barriers to long-range conduction near the oxygen vacancy adjacent to the dopant. More detailed studies including transitions at intermediate distances away from the vacancy are needed to reveal the impact of an oxygen vacancy adjacent to one dopant ion. Still, these initial studies support the findings of Kim et al.<sup>9</sup> that forming vacancy dopant clusters can suppress proton trapping by the dopant in some systems. Our work shows that the details vary. The barrier decrease near the vacancy depends on the specific type of move and the type of dopant ion. In the case of very small ions, there can in fact be a barrier increase. Our findings also support those of Takahashi et al.<sup>11</sup> whose studies revealed that the distribution of protons is affected by having a vacancy adjacent to the scandium dopant.

Recently, Yamazaki et al.<sup>34</sup> found that oxygen affinity is an excellent predictor of proton trapping and hence conductivity. They defined oxygen affinity as the energy released upon oxygen ion insertion into a vacancy site close to the dopant. Our work shows that the octahedral tilting flexibility of the lattice affects the ability of nearby oxygen ions to hydrogen bond with hydroxyls and hence their ability to act upon their affinity or attraction to protons. This results in changing both local energies and barriers. This octahedral tilting flexibility is a way that the dopant shapes the proton and oxygen vacancy conduction landscape. The oxygen vacancy further alters the proton conduction landscape near it.

# AUTHOR INFORMATION

## Corresponding Author

Maria A. Gomez — Department of Chemistry, Mount Holyoke College, South Hadley, Massachusetts 01075, United States; orcid.org/0000-0002-1098-7721; Email: magomez@mtholyoke.edu

#### **Authors**

Ziqing Lin — Department of Chemistry, Mount Holyoke College, South Hadley, Massachusetts 01075, United States Shiyun Lin — Department of Chemistry, Mount Holyoke College, South Hadley, Massachusetts 01075, United States Yuan Tian — Department of Chemistry, Mount Holyoke College, South Hadley, Massachusetts 01075, United States

Alice Van Bokkelen – Department of Chemistry, Mount Holyoke College, South Hadley, Massachusetts 01075, United States

Maryann Valerio – Department of Chemistry, Mount Holyoke College, South Hadley, Massachusetts 01075, United States

Complete contact information is available at: https://pubs.acs.org/10.1021/acs.jpcc.0c09461

#### Notes

The authors declare no competing financial interest.

# ACKNOWLEDGMENTS

The research was supported by the National Science Foundation under Grant DMR-1709975 and the Mount Holyoke College Department of Chemistry. Computational resources were provided in part by the MERCURY consortium under NSF Grant CHE-1626238. We thank Frederick G. Haibach for many helpful discussions and comments.

# **■ REFERENCES**

- (1) Kreuer, K. D. Proton-conducting oxides. *Annu. Rev. Mater. Res.* **2003**, 33, 333–359.
- (2) Kreuer, K. D.; Adams, S.; Munch, W.; Fuchs, A.; Klock, U.; Maier, J. Proton conducting alkaline earth zirconates and titanates for high drain electrochemical applications. *Solid State Ionics* **2001**, *145*, 295–306.
- (3) Gomez, M. A.; Liu, F. Protons in Al doped BaZrO<sub>3</sub> escape dopant traps to access long range proton conduction highways. *Solid State Ionics* **2013**, 252, 40–47.
- (4) Yamazaki, Y.; Blanc, F.; Okuyama, Y.; Buannic, L.; Lucio-Vega, J. C.; Grey, C. P.; Haile, S. M. Proton trapping in yttrium-doped barium zirconate. *Nat. Mater.* **2013**, *12*, 647–651.
- (5) Krueger, R.; Haibach, F.; Fry, D.; Gomez, M. Centrality measures highlight proton traps and access points to proton highways in kinetic Monte Carlo trajectories. *J. Chem. Phys.* **2015**, *142*, 154110.
- (6) Buannic, L.; Sperrin, L.; Dervisoglu, R.; Blanc, F.; Grey, C. P. Proton distribution in Sc-doped BaZrO<sub>3</sub>: a solid state NMR and first principle calculations analysis. *Phys. Chem. Chem. Phys.* **2018**, 20, 4317–4328.
- (7) Ding, J.; Balachandran, J.; Sang, X.; Guo, W.; Anchell, J. S.; Veith, G. M.; Bridges, C. A.; Cheng, Y.; Rouleau, C. M.; Poplawsky, J. D.; et al. The Influence of Local Distortions on Proton Mobility in Acceptor Doped Perovskites. *Chem. Mater.* **2018**, *30*, 4919–4925.
- (8) Oikawa, I.; Takamura, H. Correlation among Oxygen Vacancies, Protonic Defects, and the Acceptor Dopant in Sc-Doped BaZrO3 Studied by 4SSc Nuclear Magnetic Resonance. *Chem. Mater.* **2015**, 27, 6660–6667.
- (9) Kim, H. S.; Jang, A.; Choi, S. Y.; Jung, W.; Chung, S. Y. Vacancy-Induced Electronic Structure Variation of Acceptors and Correlation with Proton Conduction in Perovskite Oxides. *Angew. Chem., Int. Ed.* **2016**, *55*, 13499–13503.

- (10) Takahashi, H.; Yashima, I.; Amezawa, K.; Eguchi, K.; Matsumoto, H.; Takamura, H.; Yamaguchi, S. First-Principles Calculations for the Energetics of the Hydration Reaction of Acceptor-Doped BaZrO3. *Chem. Mater.* **2017**, 29, 1518–1526.
- (11) Takahashi, H.; Oikawa, I.; Takamura, H. Atomistic Insight into the Correlation among Oxygen Vacancies, Protonic Defects, and the Acceptor Dopants in Sc-Doped BaZrO3 Using First-Principles Calculations. *J. Phys. Chem. C* **2018**, *122*, 6501–6507.
- (12) Gomez, M. A.; Chunduru, M.; Chigweshe, L.; Foster, L.; Fensin, S. J.; Fletcher, K. M.; Fernandez, L. E. The effect of yttrium dopant on the proton conduction pathways of BaZrO<sub>3</sub>, a cubic perovskite. *J. Chem. Phys.* **2010**, *132*, 214709.
- (13) Gomez, M. A.; Shepardson, D.; Nguyen, L. T.; Kehinde, T. Periodic long range proton conduction pathways in pseudo-cubic and orthorhombic perovskites. *Solid State Ionics* **2012**, *213*, 8–13.
- (14) Gomez, M. A.; Kwan, G.; Zhu, W.; Chelliah, M.; Zuo, X.; Eshun, A.; Blackmer, V.; Huynh, T.; Huynh, M. Ordered yttrium concentration effects on barium zirconate structure, proton binding sites and transition states. *Solid State Ionics* **2017**, *304*, 126–134.
- (15) Glazer, A. M. The classification of tilted octahedra in perovskites. *Acta Crystallogr., Sect. B: Struct. Crystallogr. Cryst. Chem.* 1972, 28, 3384.
- (16) Gomez, M. A.; Fry, D.; Sweet, M. Effects on the proton conduction and limiting barriers and trajectories in BaZr<sub>0.875</sub>Y<sub>0.125</sub>O<sub>3</sub> due to the presence of other protons. *Han'guk Seramik Hakhoechi* **2016**, 53, 521–528.
- (17) Kresse, G.; Furthmüller, J. Efficient iterative schemes for *ab initio* total-energy calculations using a plane-wave basis set. *Phys. Rev. B: Condens. Matter Mater. Phys.* **1996**, *54*, 11169–11186.
- (18) Kresse, G.; Joubert, D. From ultrasoft pseudopotentials to the projector augmented-wave method. *Phys. Rev. B: Condens. Matter Mater. Phys.* **1999**, *59*, 1758–1775.
- (19) Kresse, G. Ab initio molekular dynamik für flüssige metalle. Ph.D. thesis, Technische Universität at Wien: 1993.
- (20) Kresse, G.; Hafner, J. Ab initio molecular-dynamics for liquid-metals. *Phys. Rev. B: Condens. Matter Mater. Phys.* **1993**, 47, 558.
- (21) Kresse, G.; Furthmüller, J. Efficiency of ab-initio total energy calculations for metals and semiconductors using a plane-wave basis set. *Comput. Mater. Sci.* **1996**, *6*, 15–50.
- (22) Henkelman, G.; Uberuaga, B. P.; Jónsson, H. A climbing image nudged elastic band method for finding saddle points and minimum energy paths. *J. Chem. Phys.* **2000**, *113*, 9901–9904.
- (23) Henkelman, G.; Jonsson, H. Long time scale kinetic Monte Carlo simulations without lattice approximation and predefined event table. *J. Chem. Phys.* **2001**, *115*, 9657–9666.
- (24) Henkelman Group, Department of Chemistry and Biochemistry, University of Texas at Austin http://theory.cm.utexas.edu/vtsttools/dymmat.html (accessed November 29, 2020).
- (25) Giannici, F.; Shirpour, M.; Longo, A.; Martorana, A.; Merkle, R.; Maier, J. Long-Range and Short-Range Structure of Proton-Conducting Y:BaZrO<sub>3</sub>. *Chem. Mater.* **2011**, 23, 2994–3002.
- (26) Cervera, R. B.; Oyama, Y.; Miyoshi, S.; Oikawa, I.; Takamura, H.; Yamaguchi, S. Nanograined Sc-doped BaZrO<sub>3</sub> as a proton conducting solid electrolyte for intermediate temperature solid oxide fuel cells (IT-SOFCs). *Solid State Ionics* **2014**, 264, 1–6.
- (27) Bilić, A.; Gale, J. D. Ground state structure of BaZrO<sub>3</sub>: A comparative first-principles study. *Phys. Rev. B: Condens. Matter Mater. Phys.* **2009**, *79*, 174107.
- (28) Bohn, H. G.; Schober, T. Electrical conductivity of high-temperature proton conductor  $BaZr_{0.9}Y_{0.1}O_{2.95}$ . J. Am. Ceram. Soc. **2000**, 83, 768–772.
- (29) Yamazaki, Y.; Hernandez-Sanchez, R.; Haile, S. M. High total proton conductivity in large-grained Yttrium-Doped Barium Zirconate. *Chem. Mater.* **2009**, *21*, 2755–2762.
- (30) Torayev, A.; Sperrin, L.; Gomez, M. A.; Kattirtzi, J. A.; Merlet, C.; Grey, C. P. Local Distortions and Dynamics in Hydrated Y-Doped BaZrO3. *J. Phys. Chem. C* **2020**, *124*, 16689–16701.

- (31) Jedvik, E.; Lindman, A.; Benediktsson, M. P.; Wahnstrom, G. Size and shape of oxygen vacancies and protons in acceptor-doped barium zirconate. *Solid State Ionics* **2015**, 275, 2–8.
- (32) Hermet, J.; Torrent, M.; Bottin, F.; Dezanneau, G.; Geneste, G. Oxide ion and proton transport in Gd-doped barium cerate: a combined first-principles and kinetic Monte Carlo study. *J. Mater. Chem. A* **2014**, *2*, 9055–9066.
- (33) Patel, M.; Zhong, J.; Gomez-Haibach, K. S.; Gomez, M. A.; King, G. Low-energy  $Sr_2MSbO_{5.5}(M=Ca$  and Sr) structures show significant distortions near oxygen vacancies. *Int. J. Quantum Chem.* **2020**, 120, e26356.
- (34) Yamazaki, Y.; Kuwabara, A.; Hyodo, J.; Okuyama, Y.; Fisher, C. A. J.; Haile, S. M. Oxygen Affinity: The Missing Link Enabling Prediction of Proton Conductivities in Doped Barium Zirconates. *Chem. Mater.* **2020**, 32, 7292–7300.